All-dielectric metamaterials: irrelevance of negative refraction to overlapped Mie resonances

N P Gandji, G B Semouchkin and E Semouchkina
Electrical and Computer Engineering Department, Michigan Technological University, Houghton, Michigan, USA

E-mail: npourram@mtu.edu

Abstract. All-dielectric metamaterials comprised of identical resonators draw a lot of attention as low-loss media providing for negative refraction, which is commonly attributed to double negativity of effective material parameters caused by overlapping of Mie resonances. We study dispersion diagrams of such metamaterials composed of dielectric rod arrays and show that bandwidths of positive and negative refraction and its type are irrelevant to negativity of effective parameters; instead, they are unambiguously defined by the shape and the location of the 2nd transmission branch in dispersion diagrams and thus can be controlled by the lattice constants.

1. Introduction

Rapid progress in the field of photonics causes increased interest in all-dielectric metamaterials (adMMs), which can be practically lossless at optical frequencies [1, 2]. In difference from conventional microwave MMs composed of complementary metallic resonators, adMMs usually consist of identical "atoms" and thus are expected to demonstrate common features with ordinary photonic crystals (PhCs). Such specifics should be accounted for at the analysis of the most intriguing phenomenon of negative refraction observed in adMMs, which are composed of Mie-type resonators [3-11]. Originally, Mie theory [12] described wave scattering by single dielectric particles (spheres or infinite rods), and its extension to resonances in arrays implied negligible interaction between particles.

Before emergence of MM concepts, it was thought that Mie resonances in PhCs could create their own photonic states with localization lengths comparable to lattice constants [13]. These states were expected to contribute to transmission due to wave transfer/hopping between neighboring resonators. Further studies [14] conveyed that respective states could define transmission branches in PhC's dispersion diagrams and even control bandgaps.

After MMs' implementation, PhCs with Mie resonances became typically viewed as MMs, complying with the effective medium theory and the Lorentz's dispersion model. Although Veselago et al. [15] expressed doubts in such views, which neglected the role of periodicity in PhCs, it became common practice to analyze adMMs' properties by using spectra of effective parameters, retrieved from scattering data for one cell [3-11]. Justification of this practice was based on the assumption that resonators' dimensions were relatively small compared to wavelengths of radiation. As the result, negative refraction in adMMs [3-11] was attributed to double negativity of effective material parameters, which could be expected at overlapping of the "tails" of electric- and magnetic-type Mie resonances, although no proofs of the "double negativity" effect and no data about the formation of hybrid modes, which had to combine electric and magnetic resonance modes in particles of one type, were presented. Serious problems with application of the effective medium concepts to the description of wave propagation in adMMs were revealed in [16], where it was proposed to relate the observed phenomenon of negative refraction to the Bragg diffraction, although no investigation of the band diagrams of respective adMMs was performed.

In this work, we investigate the origin of negative refraction in adMMs by analyzing their dispersive properties defined by the structure periodicity, along with Mie resonances. The objects of our studies were represented by 2D arrays of infinitely long round dielectric rods. The diameters of rods and the properties of rod dielectrics were taken similar to those used in either [3] or [11] to represent the range of parameters covered by the set of works [3-11]. In particular, relative dielectric permittivity of rods ε_r was taken equal to either 100 or to 600. As in all works of this set, TM wave incidence, with E-field directed along the axes of rods and wave propagation vector (k-vector) normal to these axes, was employed.

2. Methodology of conducted studies

To simulate electromagnetic responses of adMMs, we employed various models of rod arrays and used various software. In particular, we worked as with the single cell models typically used for characterizing homogenized MMs (figure 1(a)), so with models better suitable for PhCs representation, such as a row of cells stacked in the k-vector direction (figure 1(b)). The row was usually composed of 5 cells as, according to [17], it was sufficient for representing PhC's response. However, models involving 9 and even 11 cells were also employed. Periodicity in the directions normal to k-vector was provided by proper boundary conditions at cell faces. Two full-wave software packages (COMSOL Multiphysics and CST Microwave Studio) were used for the studies of S-parameter spectra, wave propagation patterns and distributions of field intensities in arrays at the resonances. CST Microwave Studio was found preferable for monitoring field distributions in cross-sections of the basic models and for obtaining spectra of S-parameters and spectra of signals from field probes used to control resonance fields in the rods. Figure 1c allows for comparing S21 spectra obtained for the single-cell model and for the model composed of 5 cells. As seen in the figure, the spectrum obtained for the latter model clearly demonstrates a set of transmission bands divided by bandgaps and thus, provides the data comparable with those resulting from dispersion diagrams, although calculation of the latter suggests infinite array samples. In difference from dispersion diagrams, S21 spectra demonstrate transmission fringes caused by Fabry-Perot (F-P) resonances characteristic for PhCs of finite size [17]. COMSOL Multiphysics software was mostly used for studying multi-cell chains representing wave processes in adMMs with close-to-zero index values (snap-shot exemplifying wave pattern in such chain is presented in figure 1(d)). Snap-shots similar to that in figure 1(d) were used to estimate wavelengths and, then, absolute index values at frequencies of interest: $|n| = \frac{c_0}{\lambda \cdot f}$. Considering figure 1(d) it is easy to ensure that the depicted snap-shot represents the wavelength of 470 microns, i.e. of 0.047 cm. Such wavelength corresponds to the absolute index value of 0.5, which is exactly the same as defined by the retrieval procedure at respective frequency of 1.28 THz (shown below in figure 2(d)). The retrieval procedure operating with S-parameter spectra was the basic one in this work for obtaining spectra of index values. For this procedure, we usually employed S-parameter spectra simulated for 5-cell models. However, one-cell models were also checked for comparison with the results in [3] and [11]. Index spectra for two types of models did not demonstrate significant differences.

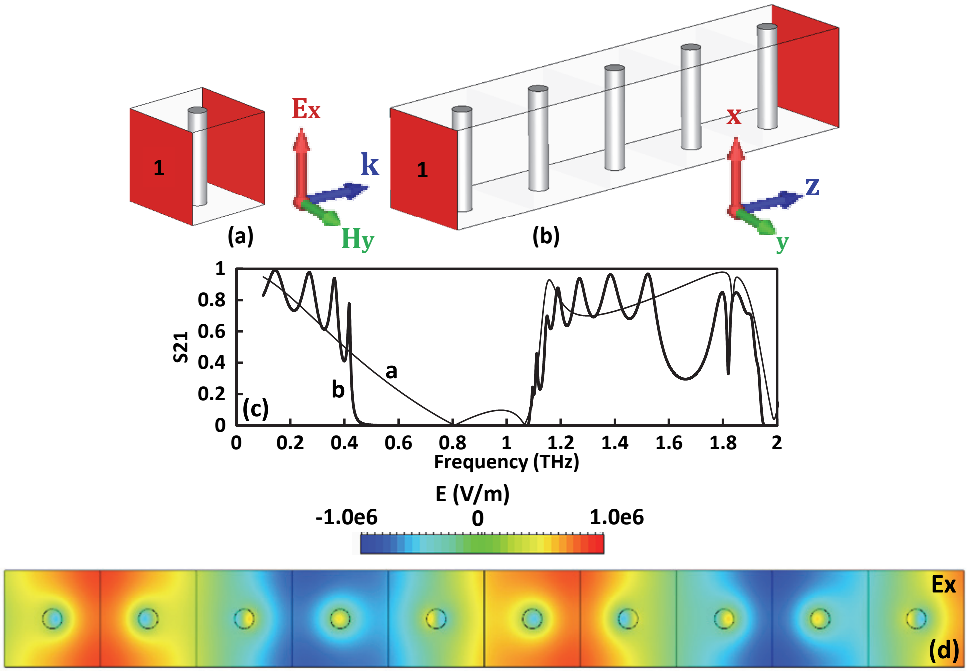

Figure 1. (a) One-cell model of adMM, (b) model of 5 stacked cells, (c) simulated S21 spectra for the models presented in (a) - thin curve, and (b) - bold curve, for 2D square-lattice rod array with ε_r=100, rod radius 10 μm, and the lattice constant α =100 μm, and (d) snap-shot of E-field intensity at wave propagation through multi-cell model of adMMs with rod and lattice parameters similar to those in (c), sampled at f=1.28 THz.

As in many other works on MMs, index retrieval was based on employing the equation given in [18]:

$$n = \frac{1}{k_0 d}\left[\left\{\left[\ln(e^{jk_0 nd})\right]'' + 2m\pi\right\} - i\left[\ln(e^{jk_0 nd})\right]'\right] \qquad (1)$$

where symbols $(\cdot)'$ and $(\cdot)''$ denote, respectively, real and imaginary parts of the refractive index, and 'm' is an integer number,

$$e^{jk_0 nd} = \frac{S_{21}}{1-\Gamma S_{11}},\ \Gamma = \frac{z-1}{z+1},\ \text{ and } z = \pm\sqrt{\frac{(1+S_{11})^2 - S_{21}^2}{(1-S_{11})^2 - S_{21}^2}} \qquad (2)$$

Correct choice of adjustable coefficient 'm' in (1) is challenging, since this coefficient has to be changed, for instance, from 0 to 1, at such frequency, at which the value m=0 causes discontinuity in the spectrum of real index component. We usually preferred to avoid such changes of coefficient 'm' and, following [19], used m=0 for the entire spectrum. However, in the cases of doubts in the accuracy of retrieved results, we controlled obtained index values by employing alternative options for index determination. It is worth noting here, that while verifying the retrieved index values, we followed [20, 21] to account properly for the effects of array periodicity on index spectra.

Obtained by using retrieval procedure index spectra along with spectra of S-parameters and probe signals were analyzed in comparison with dispersion diagrams of infinite rod arrays and with spectra of Mie resonances in single infinitely long dielectric rods. For calculation of dispersion diagrams, we used the latest editions of MPB software developed at MIT [22]. This software was also employed for calculating equi-frequency contours (EFCs), which were basically used for distinguishing bands with positive and negative indices. In addition, EFCs were used for verifying the retrieved index values. Spectra of Mie resonances were calculated by using the expression for scattering coefficients from [12]:

$$b_n = \frac{\sqrt{\varepsilon_r} J_n(k_0R) J_n'(\sqrt{\varepsilon_r} k_0 R) - J_n(k_0R) J_n'(\sqrt{\varepsilon_r} k_0 R)}{\sqrt{\varepsilon_r} H_n(k_0R) J_n'(\sqrt{\varepsilon_r} k_0 R) - H_n'(k_0R) J_n(\sqrt{\varepsilon_r} k_0 R)} \tag{3}$$

where k_0 is wavenumber in free space, R is the radius and ε_r is relative permittivity of rods, J_n and H_n represent Bessel function of the first kind and Hankel function of the second kind, respectively, while Lagrange's notation $(\cdot)'$ is used here to denote first derivatives of these functions.

3. Surface resonances in energy bandgaps versus Mie resonances

Figure 2 presents a set of spectra, described in Section II, for an adMM represented by a square lattice of rods with radius R=10 μm and relative permittivity ε_r=100, at lattice constant 100 μm. Similar adMM in [11] demonstrated negativity of real index values in the retrieved index spectra at about 1.1 THz. As seen in figure 2(a), dispersion diagram of this array features as separated by bandgaps transmission branches, so independent on k-vector photonic states at frequencies 1.15 THz and 1.82 THz, which are close to characteristic frequencies for coefficients ($|b_1|$) and ($|b_2|$), defined by (3), in the spectrum of Mie resonances of a single rod (figure 2(b)). These coefficients correspond to the magnetic resonance and to the higher order resonance, respectively [12], for which characteristic simulated field patterns are shown in inserts above figure 2(b). Similar independent on k-vector photonic states, which could be also related to Mie resonances, were observed in dispersion diagrams of 3D arrays composed of dielectric spheres and were called "localized states" [23].

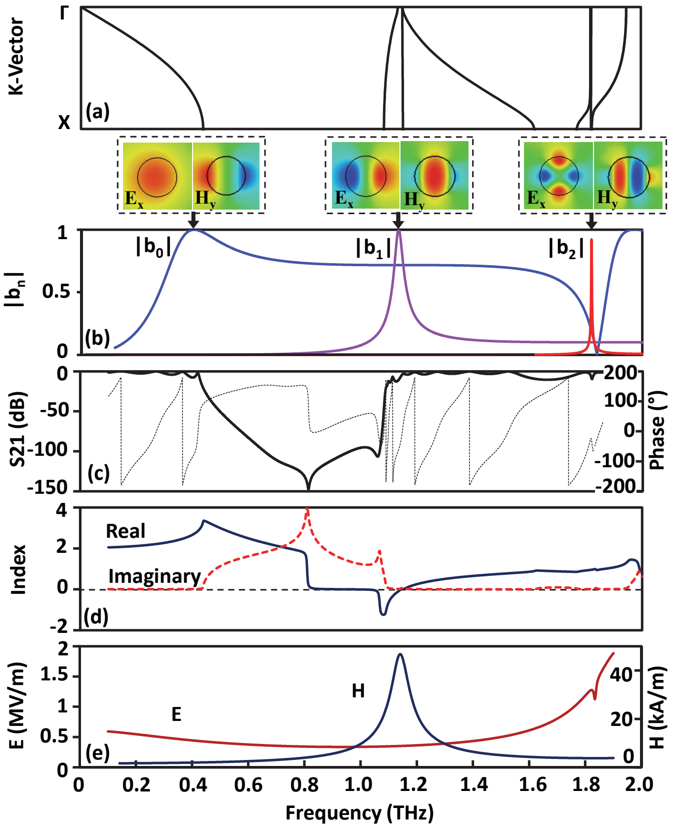

Figure 2. Spectral characteristics obtained for models of 2D square-lattice rod array with ε_r=100, R=10 μm, and lattice constant 100 μm: (a) dispersion diagram for infinite array, (b) Mie scattering by a single rod (inserts show field patterns at the maxima of Mie coefficients), (c) S21 magnitude (solid curve) and phase (dashed curve) for the model of five cells in a row, (d) retrieved index components for one-cell model, and (e) signals from E- and H-field probes in one-cell model.

No localized states, which could be associated with electric-type Mie resonance were observed as in our studies, so in [23]. The electric Mie resonance represented by the coefficient $|b_0|$ in figure 2(b) could be associated only with the position of fundamental band edge. Figures 3(a) and 3(b) present, respectively, E- and H-field patterns in the array cross-section at the frequency of band edge. Field patterns in each cell look corresponding to the patterns observed at the electric Mie resonance in a single rod (first insert above figure 2(b)). However, in neighboring cells, they demonstrate 180° phase difference that allows for relating the respective transmission mode to the odd type. In addition, field magnitude is changing from cell to cell along the chain with maximal fields observed in the third cell. These changes can be related to the formation of F-P resonance, which are common for PhCs of restricted lengths [18]. As known, F-P resonances cause formation of standing waves, and figures 3(a) and (b) just represent the snapshots of the half-wavelength standing wave. Conserved at F-P resonance out-of-phase arrangement of neighboring Mie resonances excludes a possibility of their meaningful effect on effective medium parameters and thus, excludes any contribution of the electric resonance in double negativity of effective parameters.

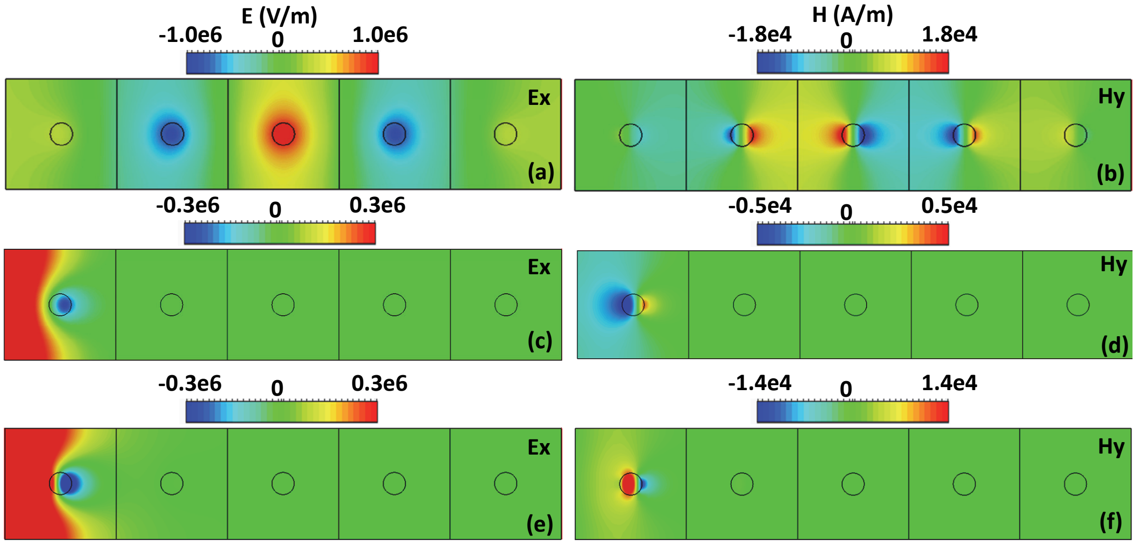

Figure 3. E- and H-field patterns in the cross-section of 2D rod array: (a)-(b) at the edge frequency of fundamental band (0.42 THz); (c)-(d) at the 1st dip in S21 spectrum (figure 2(c) - 0.8 THz); (e)-(f) at the 2nd dip in S21 spectrum (1.05 THz).

As seen in figure 2(c), S21 spectrum of the respective rod array demonstrates two dips at 0.8 THz and 1.05 THz. Similar dips were observed in S-parameter spectra by authors of [3-11], and in some cases were assumed to be related to Mie resonances in rods. However, comparison of figures 2(b) and 2(c) does not support such assumption. In addition, it can be seen from comparison of figures 2(a) and 2(c) that resonance-type dips in S21 are observed at frequencies corresponding to the bandgap in the dispersion diagram, when waves should not penetrate inside the array. Furthermore, the spectra of signals from E- and H-field probes (figure 2(e)) do not demonstrate typical for resonances enhancement of field magnitudes at dip frequencies. Field patterns in figures 3(c)-3(f) confirm that at dip frequencies, evanescent waves do not penetrate further than the first cell, where they cause weak responses barely comparable with resonance fields. This means that wave phenomena, which occur at the dips, could only be related to responses in the surface layer and not to resonance phenomena in the array volumes. It is worth noting here that observed distortions of surface responses against the patterns in inserts, placed above figure 2(b), could be caused by interaction between resonance fields at two Mie resonances. As seen in figure 2(d), this interaction reveals itself in overlapping of frequency ranges, in which imaginary components of index at two "dip resonances" are defined.

4. Refraction controlled by dispersion of transmission branches

After establishing irrelevance of surface resonances to wave phenomena in the volume of 2D rod arrays, we had to exclude from further consideration those parts of the retrieved index spectra, which were defined by surface responses due to rod interaction with evanescent waves. To do that, we took into consideration only those areas of the spectra of real index component, in which imaginary component was equal to zero, i.e. in which the index had physically meaningful values. In addition, we restricted our analysis by the frequency range around 1.1 THz, since, according to [11], negative refraction for arrays under study was expected just in this range. Our data presented in figure 2(d) for arrays with the lattice constant *a* =100 μm demonstrate a region with negative values of real index component just below 1.1 THz that agrees with the results in [11]. In order to clarify the reasons for appearance of index negativity, we compared changes in the dispersion diagrams and in the retrieved index spectra at decreasing the array lattice constant from 120 μm down to 80 μm. As seen in figure 4, at *a* =120 μm the values of real index component near 1 THz have positive sign and are defined in relatively wide band from 0.95 THz up to 1.07 THz. At *a* =110 μm, these values remain positive, however, in a narrower band between 1.04 THz and 1.1 THz. At *a* =105 μm, the band with positive indices disappears and a trend of switching to a negative index is observed at 1.08 THz. Further decrease of lattice constant leads to formation of a band, in which the values of real index component are negative. While at *a* =100 μm this band can be found between 1.08 THz and 1.12 THz, then at *a* =90 μm it extends from 1.08 THz to 1.17 THz and remains almost unchanged at *a* = 80 μm.

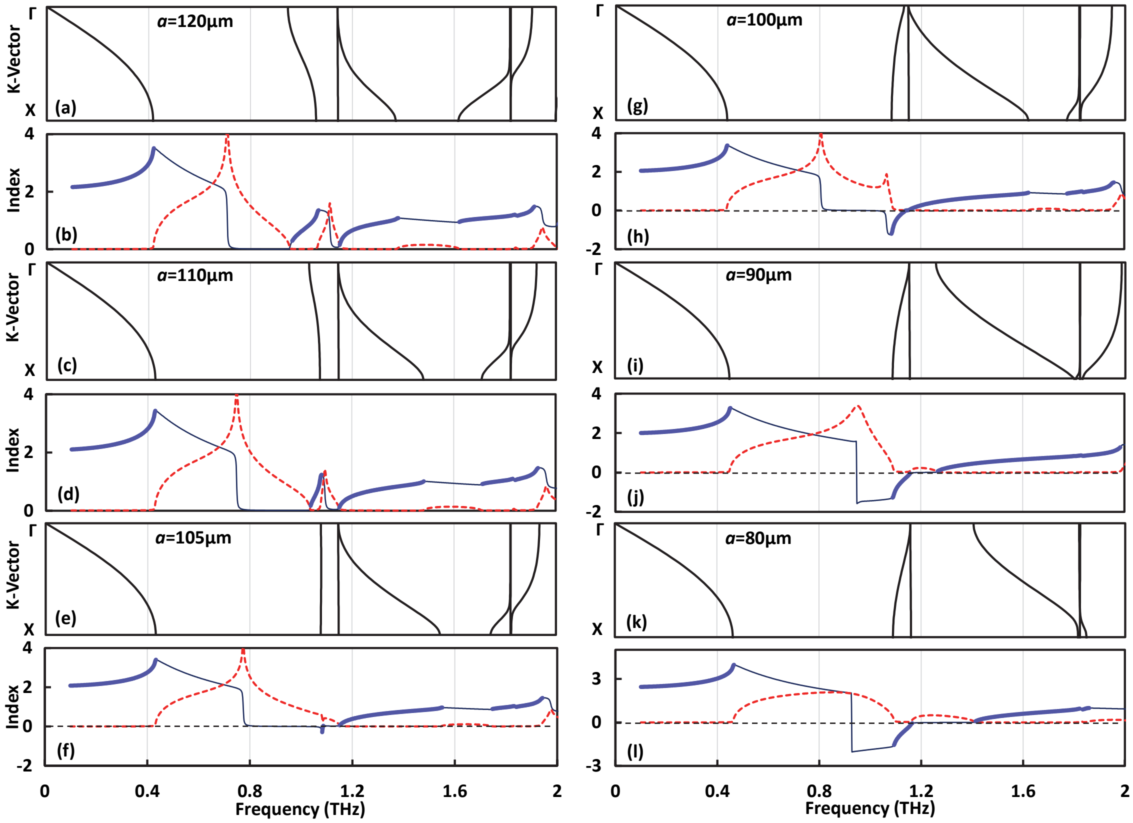

Figure 4. Dispersion diagrams and spectra of real (solid curves) and imaginary (dashed curves) index components obtained for the models of 2D rod arrays (ε_r=100 and R=10 μm) at various array lattice constants *a* in the range from 120 μm to 80 μm: (a)-(b) 120 μm, (c)-(d) 110 μm, (e)-(f) 105 μm, (g)-(h) 100 μm, (i)-(j) 90 μm, (k)-(l) 80μm.

It is well seen in figure 4 that described above bands with physically meaningful index values exactly coincide with the bands, in which the dispersion diagrams of arrays with respective lattice constants exhibit the 2nd transmission branch. Additionally, it is well seen that at 120 μm > *a* > 105 μm, the 2nd branch has the slope corresponding to positive indices, at *a* =105 μm it becomes flat, and at 105 μm > *a* > 80 μm it acquires a slope corresponding to negative indices. It should be noted here that the bands in figure 4, in which physically meaningful indices are defined, have no relation to surface resonances, since the latter affect index components in frequency ranges located far from these bands. Index spectra observed at *a* = 80 µm in [11] did not correspond neither to changes of the dispersion diagram (figure 4(k)), nor to index spectra presented in figure 4(l). This discrepancy could possibly be caused by employing a step-function for adjustable coefficient ‘m’ in [11] in the expression used for index retrieval.

Although obtained changes of retrieved index spectra at decreasing the lattice constant of the array exactly corresponded to respective changes of the 2nd branch shape, we decided to additionally verify obtained index data by using another well-known approach [23,24], taking into account mentioned above discrepancy with the data in [11]. In particular, we calculated and compared EFCs for adMM with *a* = 100 µm in 2nd and 3rd bands located just below and above 1.17 THz (see figure 4(g)) and characterized in retrieved spectrum (figure 4(h)) by negative and positive indices, respectively. We also compared EFCs for adMM with *a* = 80 µm in the fundamental and 2nd bands observed below and above the bandgap (figure 4(k)) and also presented in retrieved index spectrum (figure 4(l)) by positive and negative indices, respectively. As seen in figures 5(a) and 5(b) for adMM with *a* = 100 µm, moving from lower to high kx or ky values along the axes of EFCs for the band below 1.17 THz leads to crossing contours for lower frequencies, while for the band above 1.17 THz, such movement, just opposite, leads to crossing contours for higher frequencies. This confirms that the band below 1.17 THz can be characterized by negative indices, while the band above 1.17 THZ - by positive indices, in correspondence with retrieved index spectra in figure 4h. EFCs presented in figures 5(c) and 5(d) for adMM with *a* = 80 µm demonstrate opposite difference between two bands chosen for comparison. In the first band, increase of k-values leads to crossing EFCs for higher frequencies, while in the 2nd band we see inverse trend. These data confirm that the lower (fundamental) band can be characterized by positive indices, while the 2nd band - by negative indices, in exact correspondence with our retrieved index spectra (and in contrary with the data in [11]).

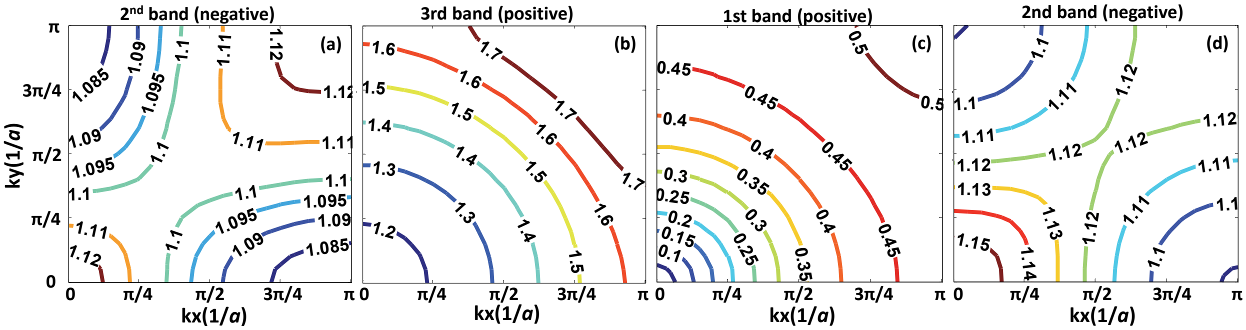

Figure 5. Equi-frequency contours in various frequency bands: (a) and (b) for adMM with a = 100 µm, (c) and (d) for adMM with a = 80 µm. (a) 2nd band, (b) 3rd band, (c) 1st band, (d) 2nd band.

5. Origin of the 2nd transmission branch in adMMs and its irrelevance to Lorentz’-type responses

The 2nd branch in the dispersion diagram, which affects the sign and the value of refractive index, needs to be considered in more details. It could be noticed that near points X of the dispersion diagrams these branches, for all used lattice constants, tend to become parallel to the branch for *a* =105 µm, which is flat and independent on k-vector. The shape of this branch makes possible its association with photonic state comparable to the localized state described in section III (observed at 1.15 THz for a =100 μm) as associated with magnetic Mie resonances in arrays. It is worth noting here that the latter state demonstrated full transmission for all arrays, while the former state observed at a =105 μm showed transmission at the level less than -50 dB that made phase changes along the rod chain unstable. This created problems for obtaining field patterns, and we were compelled to compare field patterns at two photonic states using arrays with a =100 μm. As seen in figures 6(a) and 6(b), photonic state at 1.15 THz, which, following [25], we called a localized state, represented coherent magnetic Mie resonances in all rods of the array. This state could be related to wave propagation with superluminal phase velocity and to the even transmission mode [26]. To characterize the second state, although the 2nd branch was not flat at a =100 μm, we used this branch near the point X in the dispersion diagram (figure 4(g)), where it still kept the same slope as that at a =105 μm. As seen in figures 6(c) and 6(d), obtained field patterns for the second state appeared corresponding to the odd transmission mode, in which incorporated local Mie resonances in neighboring rods were shifted in phase by 180°.

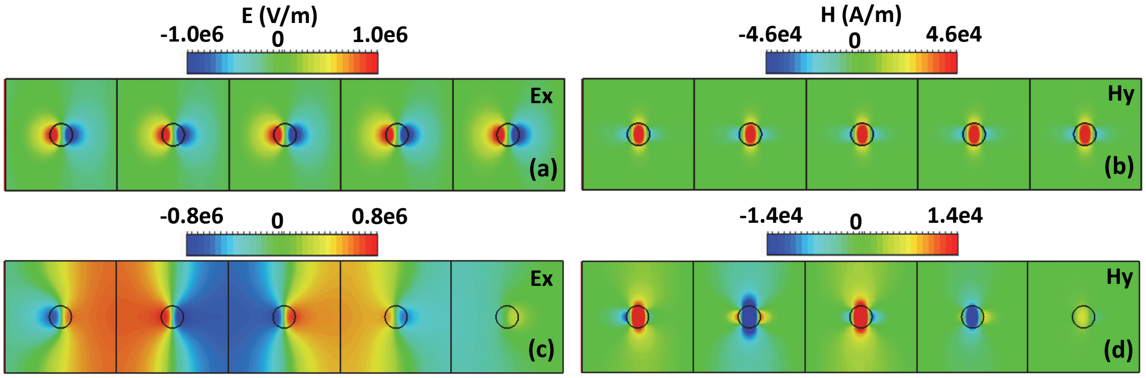

Figure 6. E- and H-field patterns in the cross-section of 2D rod array with a =100 μm: (a)-(b) at the frequency of localized photonic state (1.15 THz); (c)-(d) at the lower edge (X-point) of the 2nd branch in the dispersion diagram.

Since both even and odd transmission modes are related to the same type of Mie resonances, the formation of two modes could be considered as the result of splitting of the resonance photonic states due to difference in energy of interaction between magnetic dipoles representing resonance responses at even and odd transverse orientations [27]. Observed transition from positive refraction in the 2nd transmission band in arrays with a >105 μm to negative refraction in arrays with smaller lattice constants apparently is also related to increased interaction between resonators.

Based on the revealed rigorous correlation between the transformation of the 2nd branch in the dispersion diagrams and the reversal of the index sign occurring at changes of the array lattice constant, it can be concluded that negative refraction in adMMs is defined by the specifics of their dispersive properties and not by double negativity of their effective parameters, as it is typically expected at observation of Mie resonances [28]. It should be noted that none of the investigated here array properties, affected by occurrence of Mie resonances, appeared related to the Lorentz-type dispersion model or to the specifics of effective material parameters defined by this model. In fact, it is simply impossible to expect that dipoles formed in rod arrays at Mie resonances and incorporated in odd transmission modes could contribute to effective medium parameters. In contrary, such contribution could be expected at even modes. However, as seen in figure 4, for lattice constants in the range 120 μm > *a* > 100 μm we observe another transmission band in dispersion diagrams above even localized states, instead of a bandgap, which should appear due to negative effective permeability at the Lorentz-type resonance response.

Considering as established the dispersive origin of negative refraction in adMMs and its irrelevance to the double negativity of effective parameters, we have also confirmed that this phenomenon is related to lefthanded wave propagation. To do this, we simulated spectra of phase changes at wave transmission through multi-cell models with different quantity of stacked cells. Such spectra can be used to demonstrate either phase delay in "longer" model compared to phase in "shorter" model, which is characteristic for forward wave propagation, or respective phase advance characteristic for backward wave propagation [29]. Figure 7 compares spectra of phase changes for models composed of 9 and 11 cells of adMM with *a* = 100 μm in the bands located below and above 1.17 THz (2nd and 3rd bands in figure 4(g)). As seen in figure, the spectrum obtained for the model composed of 11 cells at frequencies corresponding to the 2nd band appears shifted forward along the frequency axis with respect to the spectrum obtained for the model composed of 9 cells. This means that at any frequency in this band, waves passing through the longer model attain phase advance with respect to waves passing through the shorter model, which is specific for the backward wave propagation. In contrast, at frequencies corresponding to the 3rd band, the phases of waves passing through the model composed of 11 cells appears delayed with respect to that for the model of 9 cells. This behavior is specific for the forward wave propagation. Thus, we can conclude that in adMM with *a* = 100 μm wave transmission in the 2nd band represents a lefthanded phenomenon.

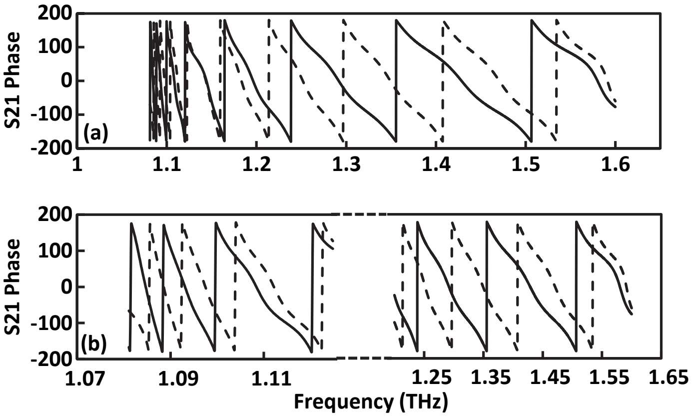

Figure 7. Spectra of phase changes at wave transmission through two models of adMM with *a* = 100 μm: (a) at the same frequency scaling in all spectra, (b) at different frequency scaling in 2nd and 3d bands to provide better resolution. In (b) the left side is related to the 2nd band, while the right side – to the 3rd band in the dispersion diagram. The model of 11 cells (dashed curves) demonstrates at the wave propagation the phase advances in the 2nd band and phase delays in the 3rd band against the model of 9 cells (solid curves).

6. Confirming the dispersive nature of negative refraction in other adMMs.

To demonstrate that our conclusions are applicable to any other rod array from referenced above publications [3-11], we present below the results of studying the dispersion diagrams and the retrieved index spectra for microwave arrays of rods used in [3, 5], taking into account that [3] is the only work, in which the phenomenon of negative refraction in adMMs was confirmed experimentally. In [3, 5], rod arrays had the lattice constant of 3 mm, the relative rod permittivity of 600 and the radius of 0.68 mm. The negative refraction was observed at frequencies around 7 GHz. Here, to ensure the possibility of realizing the same, as in figure 4 effects of lattice changes on the array properties, the values of array lattice constants were varied from 15 mm down to 3 mm.

As seen in figure 8, dispersion diagrams of all arrays incorporated, similar to that in figure 4, two localized photonic states, the lower of which slightly changed its position from 6.8 GHz at a = 15 mm up to 7.25 GHz at a = 3 mm, while the upper one remained located at the same frequency of 11 GHz. As in the previously considered case, the frequencies of localized states could be associated with the magnetic and the higher order Mie resonances in separate rods. No localized states, which could be related to electric-type Mie resonances, were found in the diagrams. As in figure 4, physically meaningful index values of arrays (registered, when imaginary index components were equal to zero) were observed at frequencies close to 7 GHz within frequency bands corresponding to the locations of the 2nd branches in dispersion diagrams.

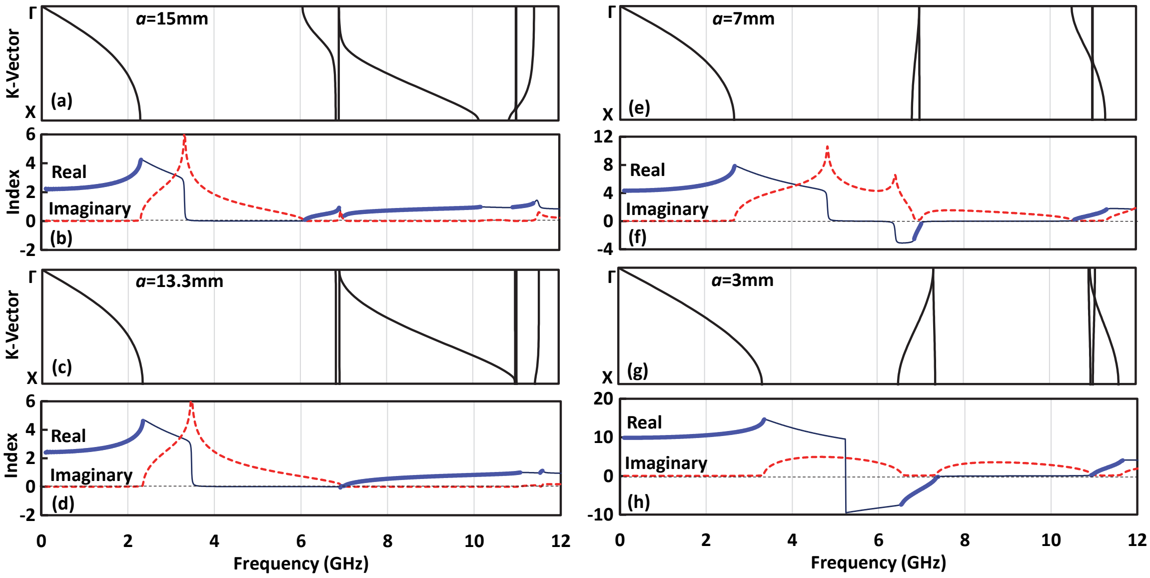

Figure 8. Dispersion diagrams and index spectra for real and imaginary components obtained for models representing 2D rod arrays (ε_r=600 and R=0.68 mm) at various array lattice constants a in the range from 15 mm to 3 mm: (a)-(b) 15 mm, (c)-(d) 3.3 mm, (e)-(f) 9 mm, (g)-(h) 3 mm.

At all lattice constants under study, the respective branches looked aligned to the lower of split photonic states associated with the magnetic Mie resonance (although, in this case, at various points of the dispersion diagram - either X or Γ), while decreasing of the lattice constant caused changes of the branch slopes with respective reversal of index sign, as well as increase of the branch bandwidth.

The obtained data additionally confirm that negative refraction in adMMs is defined by their dispersion properties, while double negativity of effective medium parameters due to Lorentz-type responses at electric and magnetic Mie resonances is irrelevant to this phenomenon.

7. Conclusion

Comprehensive studies of appearance of negative refraction in adMMs at changes of their lattice parameters have shown that there are no signs that Mie resonances cause Lorentz-type response of adMMs' effective parameters and their switching from positive to negative values. Thus, there are no data allowing for relating negative refraction to double negativity of effective parameters. Instead, strict correlation was observed between appearances of bands with negative refraction and respective transformations of 2nd transmission band in energy diagrams of adMMs at changes of their lattice constants. Obtained data allowed for concluding that the bandwidths of both positive and negative refraction in adMMs are unambiguously defined by the shape and the location of 2nd branch in dispersion diagrams and thus could be governed by lattice constants. This conclusion provides an important guidance for controlling the property of refraction in low-loss adMMs at various photonic applications.

Acknowledgments

This work was supported by the National Science Foundation under Award ECCS-1709991.

References:

[1]. Corbitt S J, Francoeur M and Raeymaekers B 2015 J. of Quant. Spec. and Rad. Trans. **158** 3-16

[2]. Jahani S and Jacob Z 2016 Nat Nano **11** 23-36

[3]. Peng L, Ran L, Chen H, Zhang H, Kong J A and Grzegorczyk T M 2007 Phys. Rev. Lett. **98** 157403

[4]. Schuller J A, Zia R, Taubner T, Brongersma M L 2007 Phys. Rev. Lett. **99** 107401

[5]. Vynck K, Felbacq D, Centeno E, Căbuz A I, Cassagne D, Guizal B 2009 Phys. Rev. Lett. **102** 133901

[6]. Lai Y J, Chen C K, Yen T J 2009 Opt. Exp.. **17** 12960-70

[7]. Peng L, Ran L and Mortensen N A 2010 Appl. Phys. Lett. **96** 241108

[8]. Wang J, Xu Z, Du B, Xia S, Wang J, Ma H, et al 2012 J. of Appl. Phys. **111** 044903

[9]. Yahiaoui R, Chung UC, Elissalde C, Maglione M, Vigneras V and Mounaix P 2012 Appl. Phys. Lett. **101** 042909

[10]. Yahiaoui R., Mounaix P, Vigneras V, Seu U C C, Elissalde C and Maglione M 2013 *Europ. Mic. Conf.* (unpublished).

[11]. Dominec F, Kadlec C, Němec H, Kužel P and Kadlec F 2014 Opt. Exp. **22** , 30492-503

[12]. Van De Hulst H C 1982 Light scattering by small particles by small particles (Dover Publications Inc.: [distributor] Grantham Book Services Ltd).

[13]. Lidorikis E, Sigalas M M, Economou E N and Soukoulis C M 1998 *Phys. Rev. Lett.* **81**, 1405-08

[14]. Lidorikis E, Sigalas M M, Economou E N and Soukoulis C M 2000 *Phys. Rev. B* **61** 13458-64

[15]. Veselago V, Braginsky L, Shklover V and Hafner C 2006 *J. of Comp. and Theor. Nano.* **3** 189-218

[16]. Valdivia-Valero F J and Nieto-Vesperinas M 2012 *Phot. Nano. Fund. Appl.* **10** 423-34

[17]. Semouchkina E, Duan R, Semouchkin G and Pandey R 2015 *Sensors* **15** 9344-59

[18]. Chen X, Grzegorczyk T M, Wu B I, Pacheco J and Kong J A 2004 *Phys. Rev. E* **70** 016608

[19]. Numan A B and Sharawi M S 2013 *IEEE Ant. and Propag. Mag.* **55** 202-11

[20]. Koschny T, Markoš P, Smith D R and Soukoulis C M 2003 *Phys. Rev. E* **68**, 065602

[21]. Koschny T, Markoš P, Economou E N, Smith D R, Vier D C and Soukoulis C M 2005 *Phys. Rev. B* **71** 245105

[22]. http://jdj.mit.edu/wiki/index.php/MIT_Photonic_BandsMPB software

[23]. Foteinopoulou S and Soukoulis C M 2003 *Phys. Rev. B* **67** 235107

[24]. Parimi P V, Lu W T, Vodo P, Sokoloff J, Derov J S, and Sridhar S 2004 *Phys. Rev. Lett.* **92** 127401

[25]. Vandenbem C and Vigneron J P 2005 J. Opt. Soc. Am. A **22** 1042-47

[26]. Semouchkina E 2012 *Metamaterial* (Intech)

[27]. Liu N and Giessen H 2010 Ang. *Chem. Int. Ed*. **49** 9838-52

[28]. Moitra P, Yang Y, Anderson Z, Kravchenko I I, Briggs D P and Valentine J 2013 *Nat. Phot.* **7** 791-5

[29]. Chen F, Wang X, Semouchkin G, and Semouchkina E 2014, *AIP Advances* **4**, 107129